

Showcasing collaborative research from the groups of Prof. Mansoo Choi at Seoul National University and Dr Hyoungchul Kim at Korea Institute of Science and Technology, Seoul, Republic of Korea.

Multiscale structured low-temperature solid oxide fuel cells with 13 W power at 500 °C

Sluggish electrode kinetics and large ohmic resistance still hinder the performance improvement of low-temperature solid oxide fuel cells (LT-SOFCs), and the ultrathin cell structure remains a greater challenge for the stability of LT-SOFCs. Herein, we report a multiscale structured LT-SOFC pertaining to high performance, long-term stability, and large-size scalability by applying ceramic micropatterning and thin-film deposition techniques. This innovative ceramic imprinting technique implements large-area microscale interfaces regardless of cell configuration and can be successfully combined with a multilayer thin-film deposition for reactive electrodes and thin electrolytes.

### As featured in:



See Mansoo Choi, Hyoungchul Kim *et al.*, *Energy Environ. Sci.*, 2020, 13, 3459.

Cite this: *Energy Environ. Sci.*,  
2020, 13, 3459

## Multiscale structured low-temperature solid oxide fuel cells with 13 W power at 500 °C†

Sung Soo Shin,<sup>abc</sup> Jeong Hun Kim,<sup>cd</sup> Kyung Taek Bae,<sup>e</sup> Kang-Taek Lee,<sup>f</sup>  
Sang Moon Kim,<sup>g</sup> Ji-Won Son,<sup>ch</sup> Mansoo Choi<sup>ib\*ab</sup> and  
Hyoungchul Kim<sup>ib\*c</sup>

Low-temperature solid oxide fuel cells (LT-SOFC) operating below 650 °C have attracted attention as a next-generation fuel cell. Although much effort has been paid to develop such fuel cells, it still remains challenging to satisfy all the requirements ensuring practical operation, such as power output and durability. Here we demonstrate 4 cm × 4 cm multiscale structured LT-SOFCs having a record high power output of 13 W per single cell at 500 °C via a large-area ceramic micropatterning and thin-film depositions. Our cell exhibits excellent long-term stability with performance degradation of less than 0.05% per 500 h. Quantitative microstructure and electrochemical analyses reveal that the proposed cell significantly lowered both ohmic and polarization losses than the reference planar cells. This work features a facile and powerful tool to implement robust and large-area 3D architectures in LT-SOFCs, which opens up opportunities to produce practical LT-SOFC systems satisfying both power and durability.

Received 19th March 2020,  
Accepted 8th June 2020

DOI: 10.1039/d0ee00870b

rsc.li/ees

### Introduction

Over the past decades, one of the major research activities for the commercialization of solid oxide fuel cells (SOFCs) as a next-generation energy platform technology has been the lowering their operating temperature. This effort has been focused on eradication of the inherent fatal flaws in SOFCs while retaining the inherent technological advantages, resulting in lower operating temperatures.<sup>1–3</sup> In particular, the low-temperature (LT) operation of SOFCs offers the following benefits in cost and

performance: (i) wider material choices for system components, (ii) rapid start-up and shutdown, (iii) lower thermal and redox cycle material stresses, and (iv) higher theoretical fuel cell efficiency (approximately twice the Carnot limit).<sup>2,4–6</sup> These features drastically improve the adoption of SOFCs in the emerging portable and transportation energy market.

Currently, the development of LT-SOFCs involves two key approaches. The first is the development and implementation of novel materials with enhanced oxygen-ion conductivity and electrode catalytic activities at low temperatures.<sup>5,7</sup> Despite the extensive efforts invested in the development of materials, the obtained materials remain incapable of achieving reasonable cell resistance at low temperatures due to their low stability and low catalytic activity.<sup>4</sup> The second approach is structural architecturing by employing thin-film and microfabrication processes. Numerous recent studies, including reducing the electrolyte thickness and increasing the reaction surface, show great potential in improving the electrochemical performance of LT-SOFCs, regardless of material limitations.<sup>8–11</sup> However, these attempts are still in the early state and many challenges, regarding specific electrochemical performance, cell scalability, and long-term stability, still need to be overcome.

Following the basic principles of a structurally architected LT-SOFC, also known as micro-SOFC, several researchers initially considered reducing the electrolyte thickness using the thin-film and microfabrication process,<sup>11–16</sup> thereby affecting the ohmic resistance. Micro-SOFCs, typically fabricated using etched silicon substrates, have attracted considerable attention for their high

<sup>a</sup> Department of Mechanical and Aerospace Engineering, Seoul National University, 1 Gwanak-ro, Seoul 08826, Republic of Korea. E-mail: mchoi@snu.ac.kr

<sup>b</sup> Global Frontier Center for Multiscale Energy Systems, Seoul National University, 1 Gwanak-ro, Seoul 08826, Republic of Korea

<sup>c</sup> Center for Energy Materials Research, Korea Institute of Science and Technology, 5 Hwarang-ro 14-gil, Seongbuk-gu, Seoul 02792, Republic of Korea. E-mail: hyoungchul@kist.re.kr

<sup>d</sup> Emerging Materials Research Section, Electronics and Telecommunications Research Institute, 218 Gajeong-ro, Yuseong-gu, Daejeon 34129, Republic of Korea

<sup>e</sup> Department of Energy Science and Engineering, Daegu Gyeongbuk Institute of Science and Technology, 333 Technojungang-daero, Daegu 42988, Republic of Korea

<sup>f</sup> Department of Mechanical Engineering, Korea Advanced Institute of Science and Technology, 291 Daehak-ro, Yuseong-gu, Daejeon 34141, Republic of Korea

<sup>g</sup> Department of Mechanical Engineering, Incheon National University, 119 Academy-ro, Yeonsu-gu, Incheon 22012, Republic of Korea

<sup>h</sup> Graduate School of Energy and Environment (KU-KIST GREEN SCHOOL), Korea University, 145 Anam-ro, Seongbuk-gu, Seoul 02841, Republic of Korea

† Electronic supplementary information (ESI) available. See DOI: 10.1039/d0ee00870b

power density owing to their innovative free-standing membrane structure composed of ultra-thin electrolytes and noble metal electrodes.<sup>11</sup> However, the mechanical fragility of the ultra-thin free-standing structure and the deterioration behaviour of the noble metal electrode led to significant stability and scalability issues, there hindering its practical application.<sup>12,13</sup> Several studies have been conducted to fabricate large electrode areas through the modified thin-film structures.<sup>12,14,15</sup> However, the low power output, which remains at tens of mW at 500 °C, as well as the other limitations, have still not been overcome.<sup>16</sup> In viewpoint of the need to increase the reactive surface area in SOFCs, only a few studies on three-dimensional (3D) structures for micro-SOFCs have been conducted. Furthermore, their surface patterning techniques have often been performed with conventional top-down fabrication processes, such as etching or laser processing.<sup>8,17</sup> In micro-SOFCs consisting of oxide substrates, achieving precise surface patterns and complex cell configurations is difficult, and their low pattern resolution and poor structural instability are obstacles to achieving high cell power output and stability.<sup>8–10,17</sup> To the best of our knowledge, no prior top-down approach including laser processing has reported significant performance enhancements. This is because of the low-resolution and low-quality characteristics of this technique which implements surface patterns by etching, melting, or evaporating thick ceramic layers.<sup>8,17</sup> In summary, conventional top-down fabrication processes have not overcome the inherent limitations of LT-SOFC resulting from the unique mechanical properties of ceramics as the core materials of SOFCs, including their brittleness and stiffness.

In this study, we developed a high-performance LT-SOFC with 3D micro/nano interface architectures, using large-area ceramic micropatterning and multilayer thin-film deposition techniques. The as-developed ceramic micropatterning process, *via* polymer-to-ceramic matrix transition, can fabricate a variety of 3D ceramic multilayer architectures. This process can be used regardless of material or cell configuration changes. Furthermore, by applying thin-film deposition techniques, we fabricated a multiscale structured LT-SOFC, with an active area of 4 cm × 4 cm, which delivers record-breaking electrochemical performance (power output and stability) in low-temperature operations. The electrochemical characteristics of multiscale structured SOFCs were quantitatively analysed using complementary tomographic, microscopic, and electrochemical impedance spectroscopy (EIS) techniques, and positive effect of 3D interface architectures on the performance of multiscale structured SOFCs was investigated. Finally, we clarified that the multiscale structured LT-SOFC prepared with large-area ceramic micropatterning and thin-film deposition is highly reproducible.

## Results and discussion

### 3D architectures with advanced ceramic micropatterning

Conventional imprinting process, which is known as one of the most popular pattern transfer techniques along with photolithography, is extensively used as an economical microfabrication process in a broad range of industries.<sup>18,19</sup> This process is

based on the basic principle of pattern creation by engraving structures onto a resin coated on a substrate with heat or ultraviolet (UV) radiation while pressing the patterned original mold or replica.<sup>20,21</sup> In particular, the imprinting process that utilizes the fluidity and mechanical deformation of a resin in high-temperature/high-pressure conditions can be performed in liquid and polymeric solid phases. Correspondingly, it has excellent versatility in the fabrication of micro- and nanoscale pattern structures with low cost and high throughput.<sup>22,23</sup> Unfortunately, some research fields that utilize ceramic materials with brittle and rigid physical properties have been unable to apply this imprinting process and have consequently not benefited from it.

To achieve the advantages of 3D architectures in ceramics, we developed the novel large-area ceramic micropatterning process using polymer-to-ceramic matrix transition and applied it to the anode substrate in SOFCs. Fig. 1a–d show the process flow for the fabrication of a multiscale structured SOFC in three steps: (i) preparation of an imprinting mold, (ii) pattern imprinting on an anode substrate, and (iii) multilayer thin-film deposition.

As shown in Fig. 1a, we obtained the first polydimethylsiloxane (PDMS) replica from a silicon master and fabricated a final polyurethane acrylate (PUA) mold using a cured PDMS replica. The final imprinting mold has an equilateral, square pyramidal pattern with an edge length of 6 μm and pitch of 4 μm (see Fig. 1e, left column). Furthermore, to implement micropatterning process to large-area SOFC, we tried to fabricate a large-area mold for enhancement of total power ( $P_{\text{total}}$ ) output. Due to the high cost of manufacturing silicon masters for polymer molds, a multi-array structured large-area PUA mold was prepared using a small-area PDMS replica. As depicted in Fig. 1b, the PUA resin can be cured in a pyramidal pattern only in the region of the transparent open window using a black mask film that blocks UV light. This process was performed sequentially to implement a large-area multi-arrayed PUA mold. Because a UV-curable PUA mold has an elastic modulus of 350–10 000 MPa, which is hundreds of times larger than PDMS, its mold patterns are not significantly deformed during the high-pressure conditions of the imprinting step.<sup>24</sup> These features of the PUA mold are advantageous for the pattern transfer process in ceramics.

Along with the preparation of the rigid imprinting molds, the substrate preparation capable of plastic deformation and particle rearrangement in the imprinting process constitutes another key process. Although tape casting is a classical ceramic processing technique, we modified the processing conditions to consider rearrangement and packing of ceramic particles suitable for the ceramic imprinting. The polyvinyl butyral binder applied in this process has a low glass-transition temperature (approximately 80 °C), similar to the thermal lamination condition of the anode tapes. Accordingly, we could simultaneously proceed with multilayer lamination of the anode tapes, and application of the ceramic imprinting on these tapes.<sup>25</sup> It also helps the rearrangement and packing of ceramic powder during lamination and subsequent heat treatment, thus ensuring that the transferred pattern structures are well maintained.

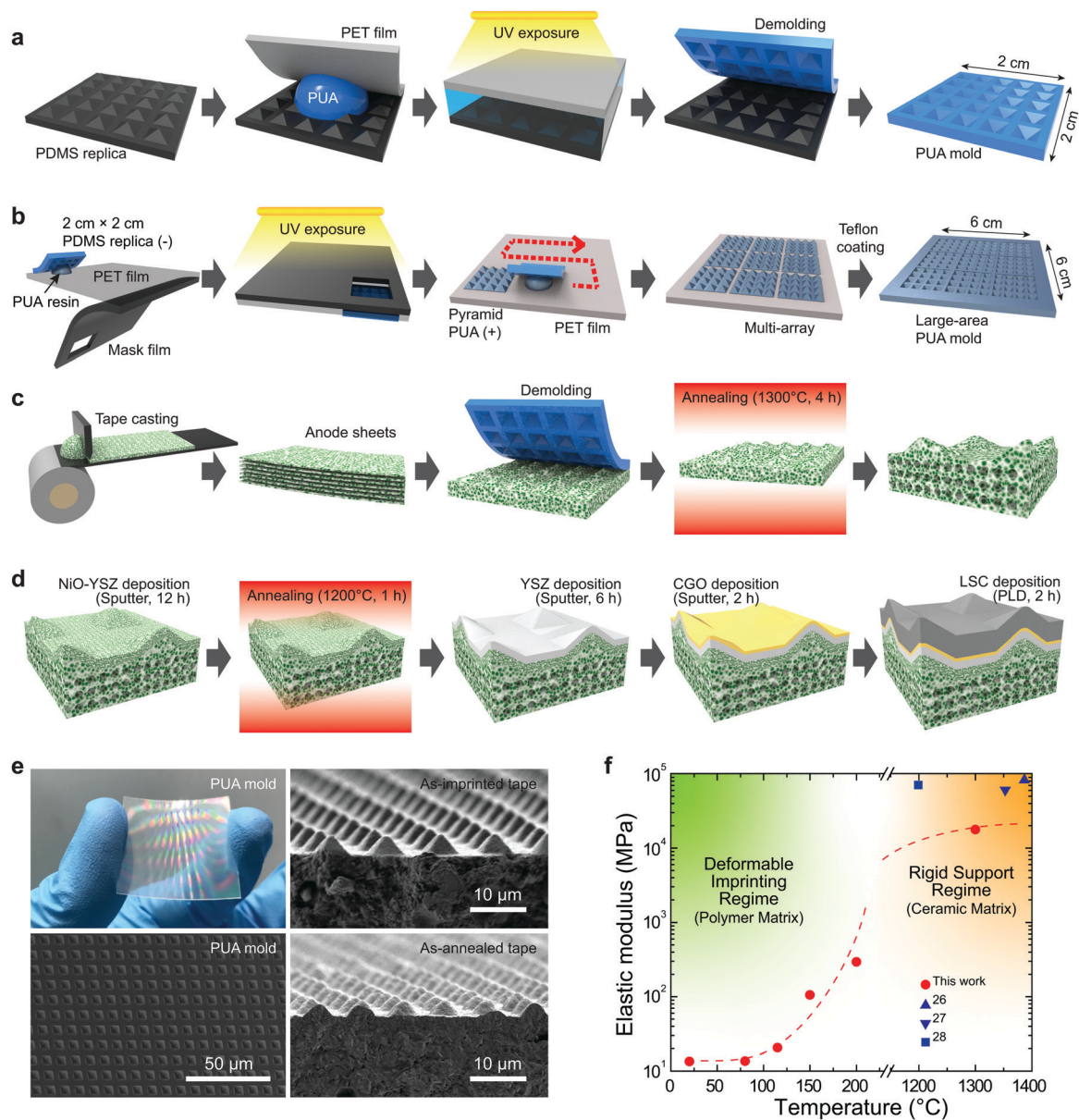


**Fig. 1** Fabrication of multiscale ceramic architectures. Schematic illustrations of the (a) preparation of PUA mold from a PDMS replica, (b) preparation of large-area multi-arrays PUA mold for large-area cells, (c) molding process used to fabricate a 3D NiO-YSZ substrate architecture, and (d) implementation of the multilayer thin-film deposition process. (e) Snapshots and SEM images of a PUA mold (left), as-imprinted NiO-YSZ anode tapes (top-right) and as-annealed NiO-YSZ anode tapes (bottom-right). (f) Variations of the elastic modulus of anode tapes with temperature.

This whole process can be explained by the principle of matrix transition and variations of the elastic modulus ( $E$ ) of anode tapes as follows. Fig. 1f shows the detailed fabrication steps of the anode tapes and the relevant elastic modulus of anode tapes using the ceramic imprinting process. The measured elastic moduli of anode tapes are in good agreement with the reported experiments<sup>26–28</sup> and clearly show the polymer-to ceramic matrix transition with respect to the processing temperature ( $T$ ). The imprinting step requiring plastic deformation has a polymer matrix ( $E \sim 10$  MPa) that dominates the mechanical properties of the anode substrate, while the green ceramic substrate ( $E \sim 20$  GPa) after the subsequent heat treatment manifests

the electrochemical properties of the ceramics. The shape of the fabricated pyramidal pattern is shown in the scanning electron microscopy (SEM) images of Fig. 1e. The figure confirms that pattern imprinting was successfully performed before and after annealing. Fig. S1 (ESI<sup>†</sup>) shows the imprinted interface with various shapes (e.g., lines and prisms). Based on these results, we can confirm that the ceramic micropatterning process is useful for fabricating microscale ceramic architectures without depending on pattern shapes.

As a final step in this process, we fabricated the diffusion-barrier layer (DBL), electrolyte, and cathode layer using thin-film deposition techniques, such as sputter and pulsed-laser

deposition (PLD), to facilitate microscale 3D architectures and maximize cell performance. As shown in Fig. 1d, the nanoscale anode-functional layer (nAFL) contains only a few pores and reduced surface roughness. This layer was deposited onto a substrate by a sputtering process for reliable deposition of a dense electrolyte layer and porous cathode layer. The nAFL, which was annealed at 1200 °C for 1 h, prevented the cracking of the electrolyte by redox cycling and particle coarsening of Ni in a reducing atmosphere and produced a substrate with fewer surface defects.<sup>29</sup> The electrolyte and DBL were then deposited with a different, subsequent, sputtering process. We finally obtained a multiscale structured SOFC based on the deposition of a  $\text{La}_{0.6}\text{Sr}_{0.4}\text{CoO}_{3-\delta}$  (LSC) cathode layer with a thickness of 3  $\mu\text{m}$  using a PLD process. To understand the structural and electrochemical characteristics of a multiscale structured SOFC, a reference cell with planar interfacial structure was also prepared in this study using the same material and processing conditions. Hereafter, we abbreviate 3D architected and reference planar-surface cells as “3DA-cells” and “Planar-cells,” respectively.

### Superior power-generating performance with 3DA-SOFCs

Fig. 2a shows the configuration and microstructure of the 3DA-cell obtained after the entire fabrication process is completed. To achieve a stable electrochemical reaction at a temperature of 500 °C or higher, we chose  $\text{Ce}_{0.9}\text{Gd}_{0.1}\text{O}_{1.95}$  (CGO) and 8 mol%  $\text{Y}_2\text{O}_3$ -stabilized  $\text{ZrO}_2$  (YSZ) as thin DBL (thickness,  $t = 200$  nm) and dense electrolyte ( $t = 1.29$   $\mu\text{m}$ ), respectively. We applied them as CGO/YSZ multilayers on the NiO-YSZ anode substrate.

Compared with the microstructure of the Planar-cell in Fig. S2a (ESI<sup>†</sup>), we clearly show that the pyramidal pattern of the 6  $\mu\text{m}$  edge length was successfully fabricated in the 3DA-cell from the anode to the cathode layers. As shown in Fig. 2b and Fig. S2b (ESI<sup>†</sup>), we tested two different SOFCs (3DA-cells and Planar-cells) and obtained their cell potential ( $V_{\text{cell}}$ ) and power density (PD) curves as a function of temperature using hydrogen and air as fuel and oxidants, respectively. The open-circuit voltage ( $V_{\text{OC}}$ ) of both cells were approximately 1.1 V. These were close to the theoretical values, and thus verified that the dense electrolyte and gas-tight sealing were successfully made. Interestingly, the 3DA-cell exhibits superior electrochemical performance, which is improved by at least 17.6–54.6% compared to the Planar-cell in the entire temperature range. At the operating temperatures of 500 and 600 °C, the 3DA-cells yield maximum power densities ( $\text{PD}_{\text{max}}$ ) of 0.523 and 1.417  $\text{W cm}^{-2}$ , while the Planar-cells yield respective  $\text{PD}_{\text{max}}$  values of 0.338 and 1.205  $\text{W cm}^{-2}$ . This 3D structure *via* our ceramic micropatterning and thin-film deposition processes can be fabricated, regardless of the material and cell configuration.

Herein, we also reproduced the electrochemical advances of these 3D structures with CGO as the electrolyte material for use in challenging LT operations. CGO materials with higher oxygen-ion conductivity at LT were chosen as the main electrolyte instead of YSZ, and an ultra-thin YSZ film was then introduced as an electron-barrier layer to suppress the leakage current of CGO in low oxygen partial pressure conditions.<sup>2</sup> Considering the final structure of this 3DA-cell in Fig. 2c, we verified that the ceramic

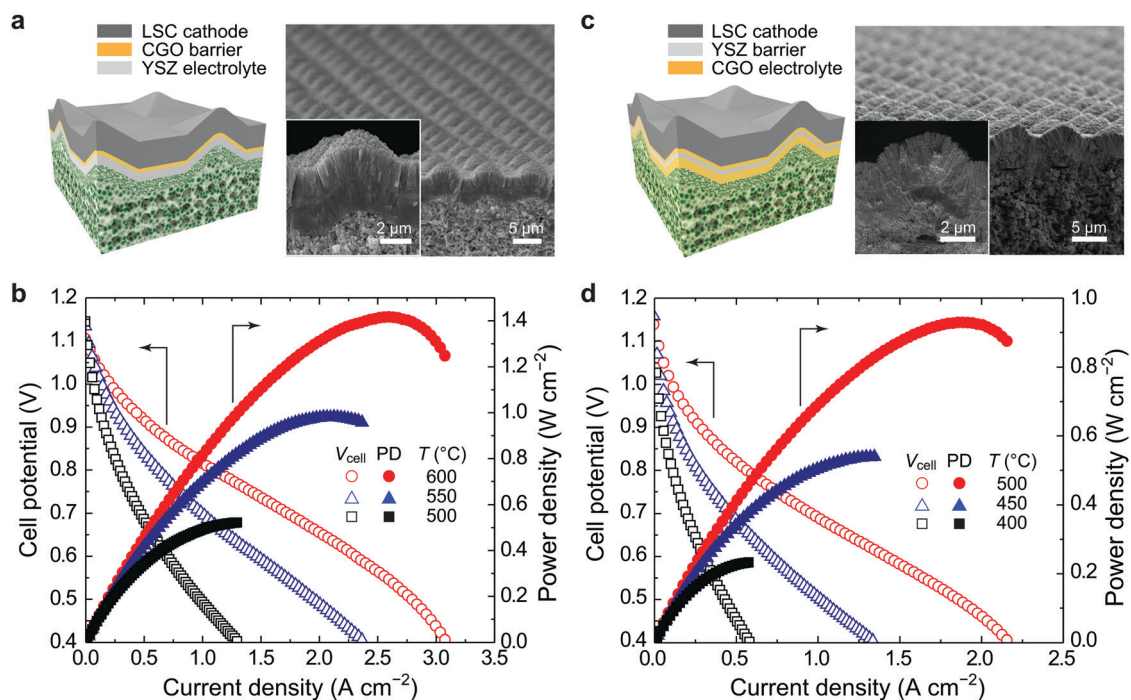


Fig. 2 Enhanced power performance of the multiscale structured SOFCs. (a) Schematic illustration (left) and SEM images (right) of a YSZ-based 3DA-cell. The inset depicts the magnified SEM image of a pyramidal structure. (b) Potential and power density curves of YSZ-based 3DA-cells at three different temperatures. (c) Schematic illustration (left) and SEM images (right) of a CGO-based 3DA-cell. The inset depicts the magnified SEM image of a pyramidal structure. (d) Potential and power density curves of CGO-based 3DA-cells at three different temperatures. All experiments were performed under a feeding of air and 3% humidified hydrogen at a rate 200  $\text{mL min}^{-1}$ .

micropatterning process facilitates fabrication of such complex configurations in a CGO-based 3DA-cell. The configuration and microstructure of this Planar-cell is also shown in Fig. S2c of the (ESI†). Fig. 2d and Fig. S2d (ESI†) show the electrochemical power-generating performance of two CGO-based cells with or without the 3D structures. This CGO-based 3DA-cell exhibits notable  $PD_{\max}$  values equal to 0.233 and 0.931  $W\ cm^{-2}$  at 400 and 500 °C, respectively, which yield better performance by approximately 21 and 17% compared to the corresponding Planar-cell at the same temperature.

### Microstructural and electrochemical analysis of 3DA-SOFCs

We investigated the origins of the excellent electrochemical performances of the 3DA-cells based on complementary tomographic, microscopic, and electrochemical analyses. The 3D reconstruction technique with focused-ion beam and SEM was first done to quantify the configuration and dimensions of the architectures of the 3D ceramic multilayers implemented in our 3DA-cells. We analyzed the 3DA-cell and the Planar-cell with respective dimensions of  $6.09 \times 6.09 \times 13.08\ \mu m^3$  and  $6.09 \times 6.09 \times 12.51\ \mu m^3$  in the  $x$ ,  $y$ , and  $z$  directions. As shown in Fig. 3a and Table 1, segmentation and reconstruction of each layer were successfully performed, and all quantitative values related to the 3D structure were obtained. As we expected, the measured surface area of a 3DA-cell was approximately 23%

larger than that of the Planar-cell. This increase in the surface area of the 3DA-cell is approximately 87% of the theoretical value (*i.e.*, overall surface area of the pyramidally shaped imprinting mold), which is reasonable considering the densification occurring in the thermal annealing process. In addition, the anode microstructure of both the cells, which was analysed quantitatively by 3D reconstruction technique, was found to be almost identical, regardless of the presence or absence of pyramidal 3D architecture, using the ceramic imprinting process, as listed in Table 1. The inset images in Fig. 3a show the pore skeleton of AFL and nAFL in both cells and suggest that pores and triple-phase boundaries (TPBs) are uniformly connected in the entire structure. To obtain the same anode microstructure of a 3DA-cell as a Planar-cell even in the high-pressure imprinting process, we prepared an AFL tape with a high green density, with its pores structure formed through the NiO reduction. The shape of the AFL layer deformed (or expanded) into a 3D pyramid shape resulted in an increase in tortuosity and small decrease in pore connectivity, but a sufficiently secured porosity and an increased active TPB length contributed positively toward the cell performance. After imprinting, by applying the same deposition conditions, it was confirmed that the nAFL formed by sputtering deposition also has the same microstructure in the final Planar- and 3DA-cells.

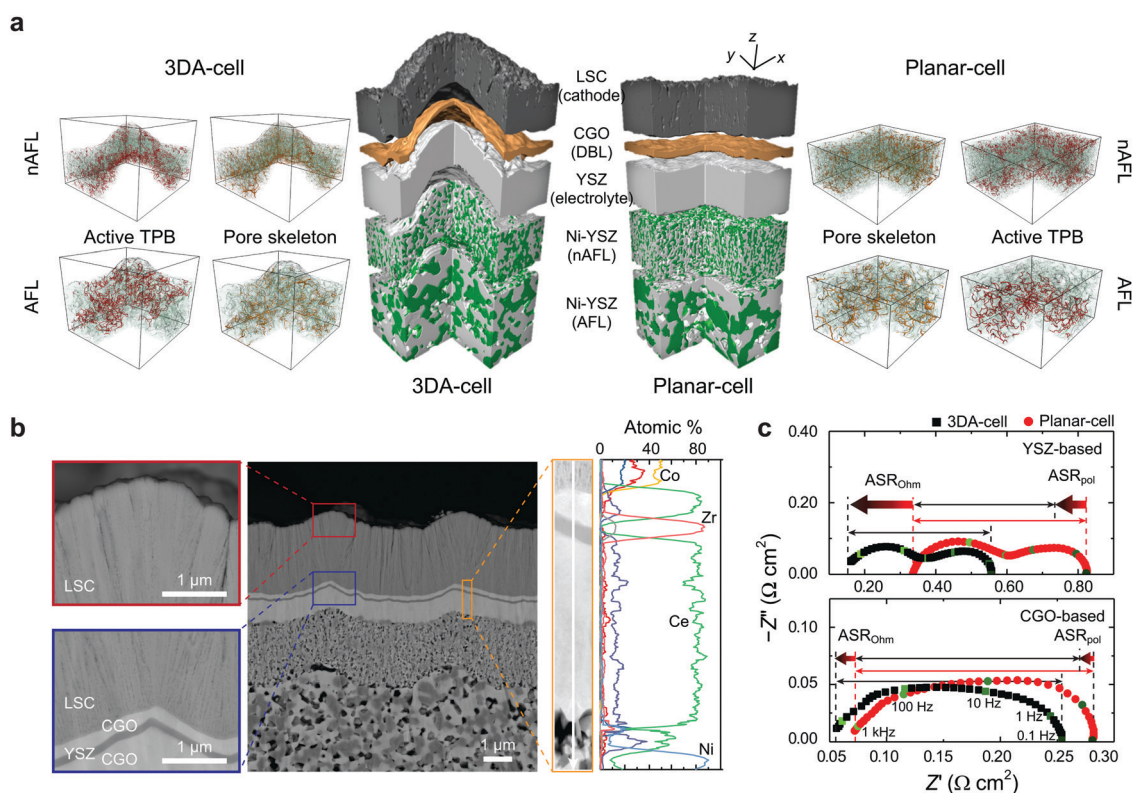


**Fig. 3** Origins of enhanced performance in multiscale structured SOFCs. (a) 3D reconstructed cell structure for one repeating unit of the compartment of a YSZ-based 3DA-cell (left) and Planar-cell (right). Magnified images of AFL and nAFL showing their pore skeleton and active TPB, respectively. (b) Cross-sectional SEM images and EDX line scans along the white line across the interfaces. (c) Measured impedance spectra of YSZ- (top) and CGO-based (bottom) 3DA-cells and Planar-cells at the cell potential of 0.75 V at 500 °C.

Table 1 Detailed microstructure information of YSZ-based 3DA- and Planar-cells verified from the 3D reconstruction technique

Cell type	Pore in AFL				Pore in nAFL				Interface area ( $\mu\text{m}^2$ )		
	Volume ratio (%)	Pore diameter (nm)	Tortuosity	Active TPB length ( $\mu\text{m}$ )	Volume ratio (%)	Pore diameter (nm)	Tortuosity	Active TPB length ( $\mu\text{m}$ )	nAFL/YSZ	YSZ/CGO	CGO/LSC
3DA	14	377.45	8.58	617.86	14	174.55	12.35	1035.65	66.37	52.08	47.68
Planar	15	339.16	5.90	377.67	11	143.23	8.23	1111.48	49.95	41.74	38.84

The microstructures of the thin-film interfaces and cathode pores were investigated using ultra-high resolution microscopic analysis techniques. We clarified the effects of improving the process reliability and cell performance associated with the 3D architectures [see Fig. 3b and Fig. S3 (ESI<sup>†</sup>)]. Since all the electrolyte layers require gas-tight properties, they are densely deposited at high temperature on nAFL with well-controlled surface roughness and pores. The post-annealing of nAFL at 1200 °C and high-temperature deposition of subsequent thin-film layers at 700 °C relieved their internal stress and suppressed massive grain coarsening, thereby eliminating any degradation issues that could occur in the cell operation step. All these processes have been verified by various cell types and material combinations in several prior literatures,<sup>29–32</sup> and their reliabilities are very high. However, the formation of conformal and homogeneous porous cathode layers on surfaces with a 3D architecture is challenging. To obtain new process conditions that are more suitable for the 3D architecture surface, we controlled the ambient oxygen pressure in PLD chamber to deposit LSC layer more densely. Under these conditions, the LSC cathode layer could be deposited as a conformal and homogeneous thin-film with macro-crack suppression. As shown in Fig. 3b and Fig. S3 (ESI<sup>†</sup>), this dense thin-film LSC layer still retains micro- and nano-pores along the columnar grain boundaries, which grow well up to the interface region that meets the electrolyte, contributing to the active oxygen-reduction reaction (ORR) of the cathode. From the viewpoint of the compositional reliability of these thin-film components and their interfacial structures, we confirmed that these are chemically reliable because no secondary phase or interfacial diffusion are observed in the line profiles of energy dispersive X-ray spectroscopy (EDX) in Fig. 3b.

We then verified that these structural changes of the 3D reaction interface were closely related to the electrochemical characteristics based on the measured EIS spectra and area-specific resistance (ASR) of each cell as a function of temperature. As shown in the EIS results of Fig. 3c, we examined the evoked effects following the increases of the interfacial area and decreases of the electrolyte thickness in 3DA-cells based on the analysis of their polarization ASR ( $\text{ASR}_{\text{pol}}$ ) and ohmic ASR ( $\text{ASR}_{\text{ohm}}$ ) responses. The  $\text{ASR}_{\text{pol}}$  value of the YSZ- and CGO-based 3DA-cells at 0.75 V was 0.395 and 0.198  $\Omega\text{ cm}^2$ , which was approximately 19 and 6% lower than those of Planar-cells (*i.e.*, 0.488 and 0.210  $\Omega\text{ cm}^2$ ). This result was attributed to the increased reaction sites of the 3DA-cell for ORR compared to the Planar-cell. Similarly, the  $\text{ASR}_{\text{ohm}}$  of the YSZ- and CGO-based 3DA-cells were 0.161 and 0.056  $\Omega\text{ cm}^2$  at 0.75 V, which was approximately 52 and 22% lower than those of the

Planar-cells (0.337 and 0.072  $\Omega\text{ cm}^2$ ). The reduction in  $\text{ASR}_{\text{ohm}}$  of the 3DA-cells results from an improvement in several ohmic resistance factors, such as the expansion of the effective area involved in oxygen-ion transfer and reduction in contact resistance at the interface, among others, with a larger surface area than the projected area. Table 2 shows the ASR values of the CGO- and YSZ-based 3DA-cells decomposed into the ohmic and polarized parts over a broad temperature range. The overall resistance of the 3DA-cell was much lower than that of the Planar-cell in every aspect, but the reduction in resistance due to the 3D interfacial effect appears to be greater in the LT region and in the ohmic part. The reduction in the polarization resistance due to the 3D interface is also more effective at LTs, but the improvement in the cell performance is limited owing to the considerable increase of polarization resistance in the LT region. The relevant EIS spectra measured at  $V_{\text{OC}}$  condition are also shown in Fig. S4 (ESI<sup>†</sup>), and these results are consistent with the existing literatures reported under similar conditions (LSC material, thin-film cathode, at 400–600 °C).<sup>32–34</sup>

#### A large-area 3DA-SOFC and its long-term stability test

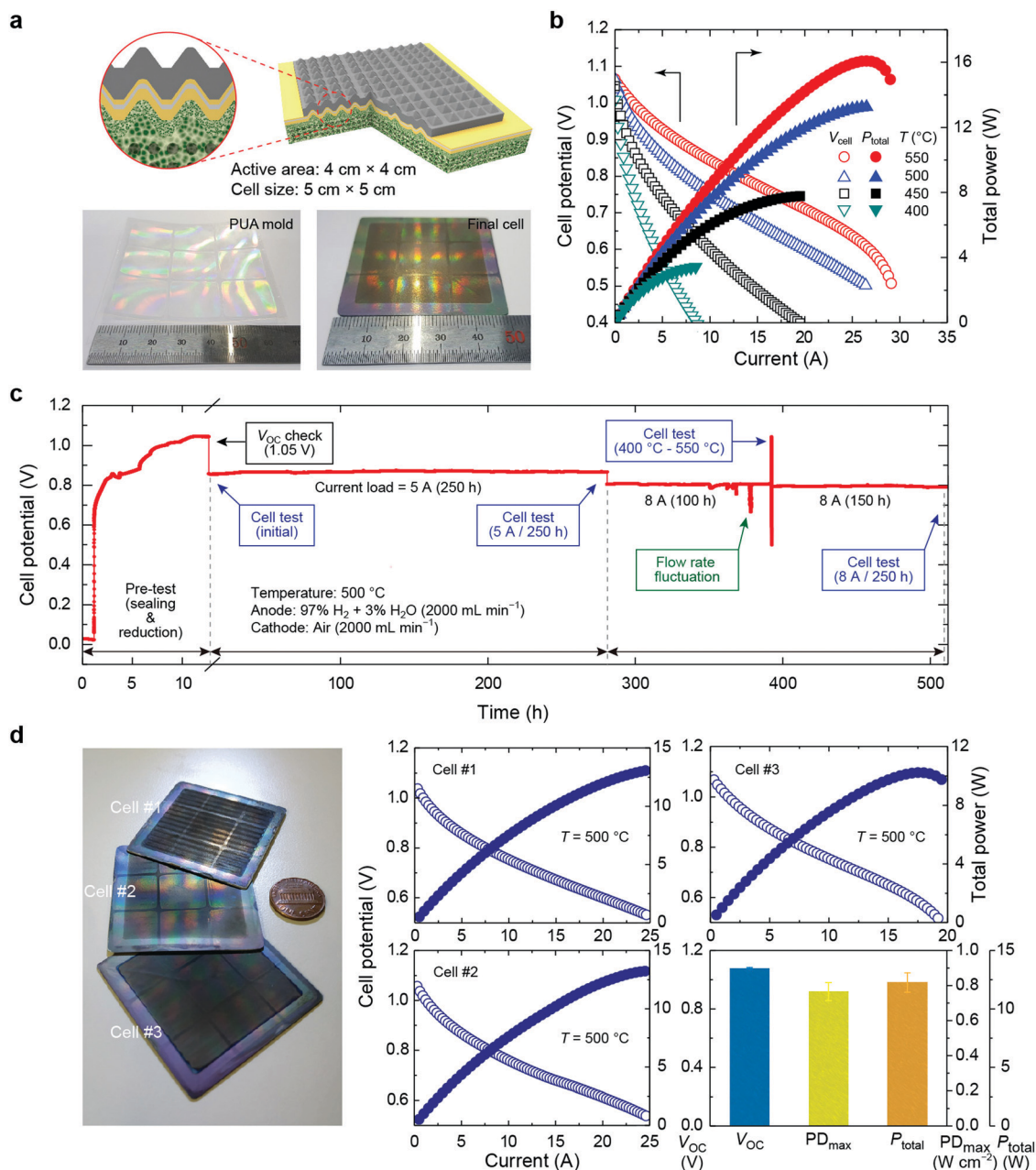
To maximize the strength of the ceramic micropatterning process, we attempted to fabricate a large-area mold and apply it to a large-area SOFC that could significantly enhance the  $P_{\text{total}}$  output. As depicted in Fig. 4a, we scale up the cell size of the 3DA-cells from a small-area cell with an active area of 1 cm × 1 cm to a large-area cell with an active area of 4 cm × 4 cm. The Inconel jig, glass-ceramic sealant, Au mesh cathode current collector, and Ni foam anode current collector used to test the large-area cell are illustrated in Fig. S5 (ESI<sup>†</sup>). As depicted in Fig. 4b, we obtained the  $V_{\text{cell}}$  and  $P_{\text{total}}$  output curves as a function of temperature using air and 3% humidified hydrogen as oxidants and fuel, respectively;  $V_{\text{OC}}$  was 1.05 V. The large-area

Table 2 Measured  $\text{ASR}_{\text{ohm}}$  and  $\text{ASR}_{\text{pol}}$  of 3DA-cells and Planar-cells at various operating temperatures. All relevant EIS spectra were measured at the  $V_{\text{cell}}$  of 0.75 V

Cell type	ASR ( $\Omega\text{ cm}^2$ )	$T$ (°C)			
		500	550	600	
YSZ-based	3DA	Ohmic	0.161	0.075	0.051
		Polarization	0.395	0.187	0.105
	Planar	Ohmic	0.337	0.146	0.072
		Polarization	0.488	0.220	0.137
			400	450	500
	CGO-based	3DA	Ohmic	0.372	0.140
Polarization			0.841	0.372	0.198
Planar		Ohmic	0.595	0.247	0.072
		Polarization	0.755	0.387	0.210

CGO-based 3DA-cell exhibited the  $P_{\text{total}}$  output of 13.27, 7.77, and 3.45 W at 500, 450, and 400 °C, respectively. The corresponding  $PD_{\text{max}}$  values were 0.829, 0.486, and 0.216 W  $\text{cm}^{-2}$  at 500, 450, and 400 °C, respectively, which are slightly lower in comparison with the small-area CGO-based 3DA-cell results (0.931, 0.539, and 0.233 W  $\text{cm}^{-2}$ ). The issues of structural and electrochemical stability of a large-area 3DA-cell, which can result from the improved cell performance, were also examined based

on long-term cell operation at 500 °C under various current load conditions. As depicted in Fig. 4c, cell performance was maintained for 250 h at a constant current condition of 5 A (*i.e.*, 0.313 A  $\text{cm}^{-2}$ ) and no apparent performance drop was observed for an additional 250 h even under the harsher constant current condition of 8 A (*i.e.*, 0.5 A  $\text{cm}^{-2}$ ). The negligible degradation rate (degradation rate = 0.05% per 500 h) during the long-term evaluation for more than 500 h demonstrated that the



**Fig. 4** Fabrication and characterization of a large-sized (active area = 4 cm × 4 cm) multiscale structured SOFC at various temperatures. All large-sized cell tests were performed under a feeding of air and 3% humidified hydrogen at a rate 2000 mL min<sup>-1</sup>. (a) Structural schematics and images of a large-area CGO-based 3DA-cell. (b) Potential and total power curves of a large-area CGO-based 3DA-cell at four different operating temperatures. (c) Recorded long-term stability test results of a large-area CGO-based 3DA-cell during a period of more than 500 h. Measured cell potential in the presence of a constant current load of 5 A for 250 h and 8 A for 250 h at 500 °C. (d) Three large-area 3DA-cells tested for the verification of reproducibility (left) and comparison of their power performance results measured at 500 °C (right). Averaged reproducibility results of large-area CGO-based 3DA-cells in terms of  $V_{\text{OC}}$ ,  $PD_{\text{max}}$ , and  $P_{\text{total}}$  are also shown.

large-area 3D multilayer architectures fabricated by our ceramic micropatterning and the thin-film deposition processes exhibited reliable results with high-stability despite the complexity of the structures. Based on these outcomes, this cell type is considered to have reasonable cell stability comparable to conventional powder-based planar-type SOFCs. In particular, most of the micro-SOFCs reported thus far have high ohmic and electrode polarization resistances, and thus need to use noble metal catalysts or adopt free-standing nanoscale membrane structures, which are considerably small in size, thereby resulting in low output, high processing cost, and extremely low cell stability.<sup>14,15</sup> By contrast, our multiscale 3DA-cells were shown to result in both high power output and high electrochemical cell stability. In addition to this excellent electrochemical performance and stability of 3DA-cells, we also comprehensively verified their experimental reproducibility by employing a large-area ceramic micropatterning and thin-film deposition. Considering the technical difficulties of high-temperature gas sealing or electrical contact in the measurement of large-area SOFCs,<sup>1,6</sup> the reproducibility confirmation is significantly challenging. In three cells with acceptable gas sealing conditions (*i.e.*,  $V_{OC}$  of 1 V or more), all large-area 3DA-cells reproduced a high power of 10 W or more; the results are summarized in Fig. 4d. The reproducibility results at 500 °C, *i.e.*, average  $V_{OC}$  of 1.08 V, average  $PD_{max}$  performance of  $0.766 \text{ W cm}^{-2}$ , and average  $P_{total}$  performance of 12.26 W, suggest that the reproducibility of 3DA-cell is sufficient. The large-area ceramic micropatterning and high reproducibility of the thin-film deposition processes discussed herein are important, but at the same time, the maturity of the elemental SOFC technologies (*e.g.*, advanced glass-ceramic compressive sealant, optimized tape-casting support, and effective current collection), which has been reported in the existing literature,<sup>25,32,35</sup> also contributed decisively to the overall cell reproducibility.

The SOFC with the 3D structure implemented in this study is an innovative achievement of ceramic processing that was accomplished based on the combination of the ceramic micropatterning and thin-film deposition processes. We successfully fabricated an SOFC with increased electrochemical performance and stability that ranged from LT to intermediate temperatures, regardless of material and cell configuration. Although there are some reports on 3D structures in the area of SOFCs,<sup>9,10,14,17</sup> our 3DA-cells are superior to those currently existing in terms of the  $P_{total}$  and degradation rate of the cell. Fig. 5 and Table S1 (ESI<sup>†</sup>) summarize the electrochemical performance of our 3DA-cells (star symbols) and the previously reported ceramic fuel cells such as SOFCs (blue region),<sup>36–45</sup> proton-conducting fuel cells (PCFCs, orange region),<sup>46–49</sup> and micro-SOFCs (green region)<sup>12,14–16</sup> in the literature with respect to various electrochemical benchmarks (*e.g.*,  $V_{OC}$ ,  $PD_{max}$ ,  $P_{total}$ , and degradation rate). To the best of our knowledge, this study achieved the highest  $P_{total}$  value among the entire ceramic fuel cells at an operating temperature approximately 500 °C, thus resulting in a 10 W-scale output. The multiscale structured LT-SOFC, which is successfully fabricated with the novel architecture and process technology, achieved new innovations in commercialization of SOFC by simultaneously securing the performance, stability, and reproducibility. We expect that the

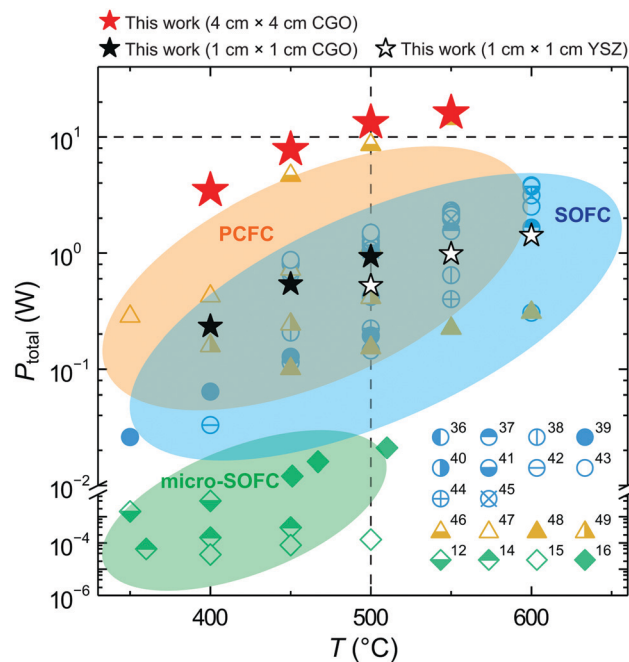


Fig. 5 Comparison of the total power performance in this work with that of the previously reported ceramic fuel cells. Some references use the area of anode substrate as active area due to the lack of information in the articles. The detailed information of each cell is listed in Table S1 (ESI<sup>†</sup>).

new processes discussed herein, especially the imprinting and sputtering processes, are commercial technologies that can be extended to a large-area cell; therefore, the mass production applicability will be excellent in the near future. The obtained power output of more than 13 W at 500 °C marked a new milestone in SOFC technology; however, further research is required to improve the cell productivity, system assembly, and operating technologies to realize SOFC commercialization that ensures economic efficiency and system reliability.

## Conclusions

In this study, we developed a high-performance LT-SOFC operating at 500 °C with 3D multiscale architectures using ceramic micropatterning and thin-film deposition techniques. Although ceramic materials have been limited in applications of the multiscale architecturing process using elastic and plastic deformation, we successfully performed the macroscale engraving of microscale interface architectures with ceramic multilayers based on the utilization of complementary polymer additives and polymer-to-ceramic matrix transition. Herein, a pyramidally shaped pattern with an edge length of 6  $\mu\text{m}$  was implemented over a small (1 cm  $\times$  1 cm) to a large active area (4 cm  $\times$  4 cm). Furthermore, the LT-SOFC with a 3D architecture was fabricated using various ways, regardless of the material and cell configurations, based on its combination with a multilayer thin-film deposition process. These cells yielded  $PD_{max}$  values that were approximately equal to  $1 \text{ W cm}^{-2}$  at 500 °C, and a performance improvement of approximately 30% compared to typical Planar-cell types using the same material and deposition process.

The quantitative analyses with the 3D reconstruction and EIS techniques showed that the increased surface area of a 3DA-cell resulted in increase of the ORR active sites and ion-conducting area. Correspondingly, the total ASR was reduced by approximately 32% compared to the planar reference cell types. Finally,  $P_{\text{total}}$  over 13 W was recorded at the operating temperature of 500 °C through the enlargement of the active area to 4 cm × 4 cm. Simultaneously, it delivered excellent cell stability for more than 500 h operation and had sufficient reproducibility with  $P_{\text{total}}$  performance (average  $P_{\text{total}}$  of 12.26 W) in three cells. Our multiscale structured SOFC fabricated herein exhibited the highest electrochemical performance in comparison to the ceramic fuel cells reported previously in terms of the various electrochemical benchmarks (*i.e.*,  $P_{\text{D}_{\text{max}}}$ ,  $P_{\text{total}}$ , and degradation rate). This work exhibits an innovative breakthrough to implement large-area microscale interfaces in ceramic fuel cells, which marks a milestone in the practical LT-SOFC systems for various applications including portable and mobile devices as well as stationary power generation.

## Author contributions

The project was conceived by S. S. S., M. C. and H. K. Sample preparation and property measurement were carried out by S. S. S., J. H. K., S. M. K., and H. K. Electrochemical characterization was performed by S. S. S., J. H. K., J. W. S., and H. K. The 3D reconstructions were performed by K. T. B. and K. T. L. The manuscript was written by S. S. S., J. H. K., M. C., and H. K. All authors discussed the results and commented on the manuscript.

## Conflicts of interest

There are no conflicts to declare.

## Acknowledgements

This work was supported by the Global Frontier R&D Program on Center for Multiscale Energy Systems funded by the National Research Foundation under the Ministry of Science and ICT, Republic of Korea (Grant No. 2012M3A6A7054855, 2015M3A6A7065442, 2014M3A6A7074784). This work was also supported in part by the Institutional Research Program of the Korea Institute of Science and Technology (2E30220). This work was also supported by the National Research Council of Science & Technology (NST) grant by the Korea government (MSIP) (No. CAP-14-01-KIST).

## References

- B. C. H. Steele and A. Heinzel, *Nature*, 2001, **414**, 345–352.
- E. D. Wachsman and K. T. Lee, *Science*, 2011, **334**, 935–939.
- N. Q. Minh, *J. Am. Ceram. Soc.*, 1993, **76**, 563–588.
- Z. Gao, L. V. Mogni, E. C. Miller, J. G. Railsback and S. A. Barnett, *Energy Environ. Sci.*, 2016, **9**, 1602–1644.
- Y. Zhang, R. Knibbe, J. Sunarso, Y. Zhong, W. Zhou, Z. Shao and Z. Zhu, *Adv. Mater.*, 2017, **29**, 1700132.
- D. J. L. Brett, A. Atkinson, N. P. Brandon and S. J. Skinner, *Chem. Soc. Rev.*, 2008, **37**, 1568–1578.
- Z. Shao and S. M. Haile, *Nature*, 2004, **431**, 170–174.
- J. A. Cebollero, M. A. Laguna-Bercero, R. Lahoz, J. Silva, R. Moreno and A. Larrea, *J. Eur. Ceram. Soc.*, 2019, **39**, 3466–3474.
- H. Seo, H. Iwai, M. Kishimoto, C. Ding, M. Saito and H. Yoshida, *J. Power Sources*, 2020, **450**, 227682.
- Y. Xu, F. Tsumori, T. Osada and H. Miura, *Micro. Nano Lett.*, 2013, **8**, 571–574.
- H. Huang, M. Nakamura, P. Su, R. Fasching, Y. Saito and F. B. Prinz, *J. Electrochem. Soc.*, 2007, **154**, B20–B24.
- J. D. Baek, C.-C. Yu and P.-C. Su, *Nano Lett.*, 2016, **16**, 2413–2417.
- I. Garbayo, D. Pla, A. Morata, L. Fonseca, N. Sabaté and A. Tarancón, *Energy Environ. Sci.*, 2014, **7**, 3617–3629.
- J. An, Y.-B. Kim, J. Park, T. M. Gür and F. B. Prinz, *Nano Lett.*, 2013, **13**, 4551–4555.
- C.-C. Chao, C.-M. Hsu, Y. Cui and F. B. Prinz, *ACS Nano*, 2011, **5**, 5692–5696.
- M. Tsuchiya, B.-K. Lai and S. Ramanathan, *Nat. Nanotechnol.*, 2011, **6**, 282–286.
- G. Cai, Y. Zhang, H. Dai, S. He, L. Ge, H. Chen and L. Guo, *Mater. Lett.*, 2017, **195**, 232–235.
- S. Y. Chou, C. Keimel and J. Gu, *Nature*, 2002, **417**, 835–837.
- S. Y. Chou, P. R. Krauss and P. J. Renstrom, *Science*, 1996, **272**, 85–87.
- G. Y. Jung, S. Ganapathiappan, D. A. A. Ohlberg, D. L. Olynick, Y. Chen, W. M. Tong and R. S. Williams, *Nano Lett.*, 2004, **4**, 1225–1229.
- H. Schulz, D. Lyebdyev, H.-C. Scheer, K. Pfeiffer, G. Bleidiessel, G. Grütznier and J. Ahopelto, *J. Vac. Sci. Technol., B*, 2000, **18**, 3582–3585.
- K. Y. Suh, Y. S. Kim and H. H. Lee, *Adv. Mater.*, 2001, **13**, 1386–1389.
- F. Zhang, J. Chan and H. Y. Low, *Appl. Surf. Sci.*, 2008, **254**, 2975–2979.
- S. M. Kim, S. M. Kang, C. Lee, S. Jang, J. Kim, H. Seo, W.-G. Bae, S. Yang and H. Yoon, *J. Mater. Chem. C*, 2016, **4**, 9608–9612.
- J. H. Kim, S. S. Shin, H. S. Noh, J.-W. Son, M. Choi and H. Kim, *J. Membr. Sci.*, 2017, **544**, 234–242.
- D. Sarantaridis, R. J. Chater and A. Atkinson, *J. Electrochem. Soc.*, 2008, **155**, B467–B472.
- S. Biswas, T. Nithyanantham, N. T. Saraswathi and S. Bandopadhyay, *J. Mater. Sci.*, 2009, **44**, 778–785.
- M. Pihlatie, A. Kaiser and M. Mogensen, *J. Eur. Ceram. Soc.*, 2009, **29**, 1657–1664.
- H.-S. Noh, J.-W. Son, H. Lee, H.-I. Ji, J.-H. Lee and H.-W. Lee, *J. Eur. Ceram. Soc.*, 2010, **30**, 3415–3423.
- C.-A. Thieu, J. Hong, H. Kim, K. J. Yoon, J.-H. Lee, B.-K. Kim and J.-W. Son, *J. Mater. Chem. A*, 2017, **5**, 7433–7444.
- K. Bae, D. Y. Jang, H. J. Choi, D. Kim, J. Hong, B.-K. Kim, J.-H. Lee, J.-W. Son and J. H. Shim, *Nat. Commun.*, 2017, **8**, 14553.
- H.-S. Noh, J. Hwang, K. Yoon, B.-K. Kim, H.-W. Lee, J.-H. Lee and J.-W. Son, *J. Power Sources*, 2013, **230**, 109–114.

- 33 E. Koep, C. Jin, M. Haluska, R. Das, R. Narayan, K. Sandhage, R. Snyder and M. Liu, *J. Power Sources*, 2006, **161**, 250–255.
- 34 J. H. Joo and G. M. Choi, *J. Power Sources*, 2008, **182**, 589–593.
- 35 J.-H. Lee, H. Kim, S. M. Kim, T.-W. Noh, H.-Y. Jung, H.-Y. Lim, H.-G. Jung, J.-W. Son, H.-R. Kim, B.-K. Kim, H.-J. Je, J.-C. Lee, H. Song and H.-W. Lee, *Adv. Energy Mater.*, 2012, **2**, 461–468.
- 36 M. Li, M. Zhao, F. Li, W. Zhou, V. K. Peterson, X. Xu, Z. Shao, I. Gentle and Z. Zhu, *Nat. Commun.*, 2017, **8**, 13990.
- 37 J. G. Lee, J. H. Park and Y. G. Shul, *Nat. Commun.*, 2014, **5**, 4045.
- 38 W. Zhou, J. Sunarso, M. Zhao, F. Liang, T. Klande and A. Feldhoff, *Angew. Chem., Int. Ed.*, 2013, **52**, 14036–14040.
- 39 C. Duan, D. Hook, Y. Chen, J. Tong and R. O'Hayre, *Energy Environ. Sci.*, 2017, **10**, 176–182.
- 40 S. Choi, S. Yoo, J. Kim, S. Park, A. Jun, S. Sengodan, J. Kim, J. Shin, H. Y. Jeong, Y. Choi, G. Kim and M. Liu, *Sci. Rep.*, 2013, **3**, 2426.
- 41 S. Yoo, A. Jun, Y.-W. Ju, D. Odkhoo, J. Hyodo, H. Y. Jeong, N. Park, J. Shin, T. Ishihara and G. Kim, *Angew. Chem., Int. Ed.*, 2014, **53**, 13064–13067.
- 42 Y.-W. Ju, J. Hyodo, A. Inoishi, S. Ida and T. Ishihara, *J. Mater. Chem. A*, 2015, **3**, 3586–3593.
- 43 J. G. Lee, M. G. Park, S.-H. Hyun and Y. G. Shul, *Electrochim. Acta*, 2014, **129**, 100–106.
- 44 Y. Chen, Y. Bu, B. Zhao, Y. Zhang, D. Ding, R. Hu, T. Wei, B. Rainwater, Y. Ding, F. Chen, C. Yang, J. Liu and M. Liu, *Nano Energy*, 2016, **26**, 90–99.
- 45 J. Kim, S. Choi, A. Jun, H. Y. Jeong, J. Shin and G. Kim, *ChemSusChem*, 2014, **7**, 1669–1675.
- 46 H. An, H.-W. Lee, B.-K. Kim, J.-W. Son, K. J. Yoon, H. Kim, D. Shin, H.-I. Ji and J.-H. Lee, *Nat. Energy*, 2018, **3**, 870–875.
- 47 C. Duan, J. Tong, M. Shang, S. Nikodemski, M. Sanders, S. Ricote, A. Almansoori and R. O'Hayre, *Science*, 2015, **349**, 1321–1326.
- 48 S. Choi, C. J. Kucharczyk, Y. Liang, X. Zhang, I. Takeuchi, H.-I. Ji and S. M. Haile, *Nat. Energy*, 2018, **3**, 202–210.
- 49 C. Xia, Y. Mi, B. Wang, B. Lin, G. Chen and B. Zhu, *Nat. Commun.*, 2019, **10**, 1707.